

Flower Inspiration: Broad-Angle Structural Color through Tunable Hierarchical Wrinkles in Thin Film Multilayers

Chao Chen, Chiara A. Airoidi, Carlos A. Lugo, R. Konane Bay, Beverley J. Glover, and Alfred J. Crosby*

The petals of some flowers form hierarchical structures when nano-scale cuticular ridges overlay bulged epidermal cells. These hierarchical structures can broaden the observable angles of iridescence. The resulting optical effect enhances the foraging efficiency of pollinators. Although efforts have been devoted to mimicking this unique broad-angle structural color, the intrinsic tunability offered by natural systems to control such a broadened spectrum is still absent in synthetic models. A hierarchical system is developed that provides hierarchical wrinkle-based structures that tune the observable angles for structural color. Laser diffraction measurements demonstrate that the observable angle of reflectance is broadened in proportion to the square root of the applied compressive strain. The morphology controls the diffraction pattern: the small wrinkles control the diffraction angles and the large wrinkles broaden the observable range. The development of a multi-mode wrinkling system to produce this broad-angle structural color only occurs within a limited range of conditions, which are experimentally discovered and theoretically modeled. Without diffractive small wrinkles, single wrinkling modes do not display structural colors. The control of wrinkling modes mimics the tunability of petals, which gives new insight into the natural system and provides a robust foundation for tunable structural color control.

colors vary with viewing angles and are referred to as iridescent.^[3,4] Structural color is ubiquitous in daily life from soap bubbles^[5] to compact discs.^[6] In nature, animals^[4] including insects,^[7–9] birds,^[10,11] and reptiles^[12] have evolved nanostructures or microstructures which generate iridescence used in signaling,^[13] thermal regulation,^[9] and camouflage.^[14] In plants, structural colors have been discovered on petals,^[6] leaves,^[15] and fruits.^[16]

Surprisingly, many structural color systems found in nature have reduced or eliminated angular dependence. In the well-known case of blue Morpho butterflies, the dorsal side of their wings appears a stunning blue structural color, nearly angle independent—a pigment-like attribute.^[7] In the case of flower petals, such as those of *Hibiscus trionum*, a broad-angle spectrum of the structural color appears in addition to the purple pigment color on the proximal part of a petal (the dark region in Figure 2a,b). This unique iridescent spectrum has been shown to

enhance the foraging efficiency of pollinators.^[6,17] Over the last decade, biomimetic designs of broad-angle iridescent materials^[18] have emerged in the field of coatings,^[19] reflective displays,^[20] optical sensors,^[21] energy harvesting,^[22] and advertising.^[23] However, these systems do not provide intrinsic tunability, which is offered by natural systems. Here, we take inspiration from how multi-mode structural color develops within flower petals to develop a robust material system, which offers structural color with an enhanced viewing angle range. We further develop quantitative models to provide understanding of our synthetic system as well as new insight into the natural systems.

1. Introduction


Structural color originates from optical interference through nanostructures or microstructures rather than molecular absorption.^[1] Typical diffraction structures include gratings (Figure 1a), photonic crystals,^[2] and multilayered thin films.^[3] The wavelengths of light that experience interference depend on the spacing of structures mediated by the incident and receiving angles. Therefore, the observable angles are distinct for a color with a particular wavelength (Figure 1a). These

2. Natural Structure and Performance

Broad-angle structural color originates from hierarchical structures that cause complex optical interference. For example, the cuticle on *H. trionum* petals^[6,24] forms nano-ridges on bulged epidermal cells (Figure 2c,d). Optical interference with the nano-ridges on the *H. trionum* petals forms near-UV structural colors, whereas the large bulged cells do not directly interfere with light, but tilt the normal direction of the nano-ridges. On

Dr. C. Chen, Dr. R. K. Bay, Prof. A. J. Crosby
Polymer Science and Engineering Department
University of Massachusetts Amherst
Amherst, MA 01003, USA
E-mail: crosby@mail.pse.umass.edu

Dr. C. A. Airoidi, Dr. C. A. Lugo, Prof. B. J. Glover
Department of Plant Sciences
University of Cambridge
Downing Street, Cambridge CB2 3EA, UK

 The ORCID identification number(s) for the author(s) of this article can be found under <https://doi.org/10.1002/adfm.202006256>.

DOI: 10.1002/adfm.202006256

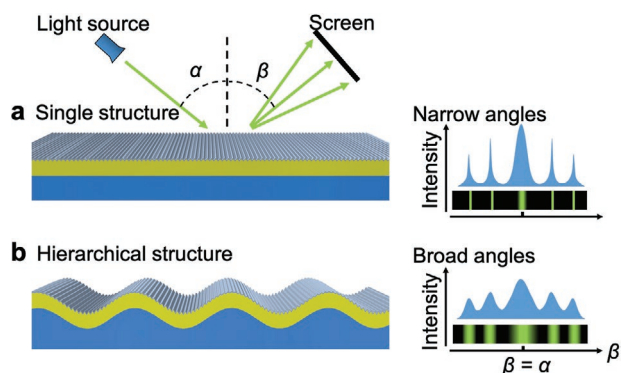


Figure 1. Schematic of the broadening mechanism of structural color by a hierarchical structure. A laser is incident to a reflective surface. The incident angle is α . The angle to receive reflection is β . a) The surface contains a diffractive periodic grating. The receiving angles of the single grating are discrete with narrow bands. b) The surface contains a hierarchical structure with two periodicities. The small structure is diffractive and the large structure broadens the receiving angles.

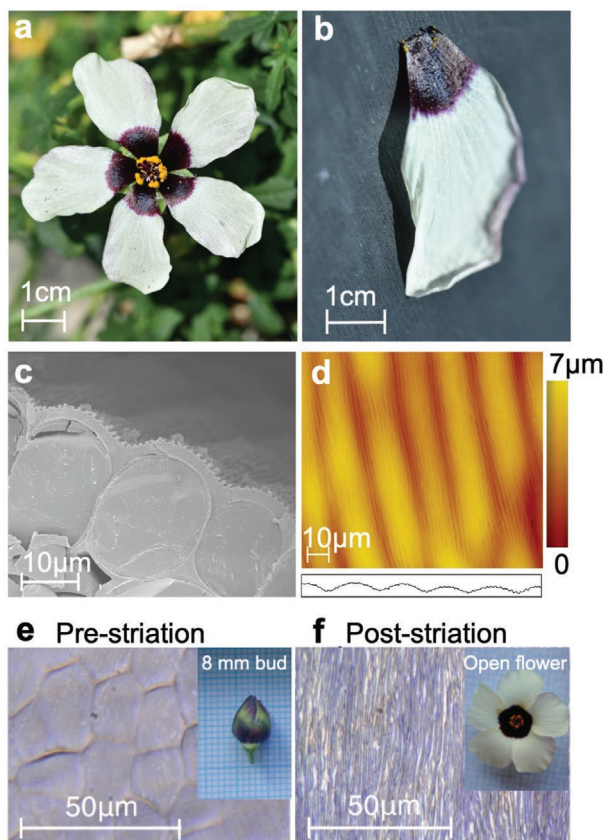


Figure 2. a) A blooming *Hibiscus trionum* flower and b) a mature petal under solar light. The surface structures on the iridescent proximal part of a mature petal through c) cryo-SEM imaging of a cross section and d) optical profilometry of the surface. The width of the optical profilometry image and the profile inset is 100 μm . The height of the profile inset is 10 μm . The microscopy images show the surface morphologies e) pre- and f) post-striation on the iridescent part of the petal. The insets show the appearance of an 8 mm-long bud whose epicalyx has been removed to reveal the size, and an open flower.

average, the receiving angle of the structural color is broadened through hierarchical structures (Figure 1b).

This wrinkle-based structural color system develops during the growth of petals, indicating the ability to dynamically tune the optical performance. Figures 2e,f show the petal surfaces before and after the formation of the nano-ridges. The epidermal cells bulge before the cuticle forms ridges. The nano-ridges initiate when the petals are closed in the flower bud and fully develop by the time the flower opens. The epidermal cells provide a natural curvature, which broadens the angle of the diffraction. The petals also demonstrate that potential pathways for tunability may exist, in that nano-ridges only form in distinct regions. The iridescent part of the *H. trionum* petal is limited to the proximal region where the cuticle forms ridges (the dark region in Figure 2b).^[6,17,24] The distal part of the petal, which lacks cuticle striation, is not iridescent (the white region in Figure 2b). We directly demonstrate a significant difference in the laser reflection patterns from these regions (Figure S1, Supporting Information). The directional reflection from the iridescent part contains a mixture of broadened diffraction signals and specular reflection, similar to previous studies.^[6,17,24] In comparison, the reflection signal from the non-iridescent white part of the petals is random.

Wrinkling, through the growth of cuticle on bulged epidermal cells,^[25] gives rise to the tunability of hierarchical structures that control the broad angle spectrum of structural color in different regions. Recent examples in the literature^[26–31] provide some of these attributes. For example, a bio-inspired structure resembling *Queen of the Night* tulip petals, formed by wrinkling a film containing a pre-etched nano-grating, mimicked the flower's iridescent effect of this flower and the angle broadening of diffraction.^[31] However, none of the previous studies integrate intrinsic multilevel developmental processes, thus limiting their tunability.

3. Synthetic Bioinspired Structure and Performance

We present the use of a precisely-defined multilayered film to develop hierarchical wrinkles that gives rise to structural color over a broad viewing angle (Figure 1b). In contrast to previous work,^[26,28,29,32–37] we utilize mechanical wrinkling of thin film multilayers to achieve efficient, complex, controlled hierarchical structures over a large area.

We fabricate the thin film multilayers through a layer-by-layer deposition^[38] as shown in Figure S2, Supporting Information. This fabrication precisely controls the thicknesses and mechanical moduli of the constituent layers (Table S1, Supporting Information). The multilayer composite is compressed uniaxially with a global compressive strain, ϵ . After compression, the multilayer surface develops intense structural colors as shown in Figure S2e, Supporting Information. We use laser reflective diffraction experiments to quantitatively study the broadening effect of the structural color as a function of materials parameters and applied compressive strain (Figure 3). The laser beam with a wavelength $\lambda_{\text{laser}} = 543 \text{ nm}$ is incident to the multilayer's surface with a fixed angle $\alpha = 45^\circ$ and a screen with a normal direction $\beta = 45^\circ$ receives the reflective signals (Figure 1). We

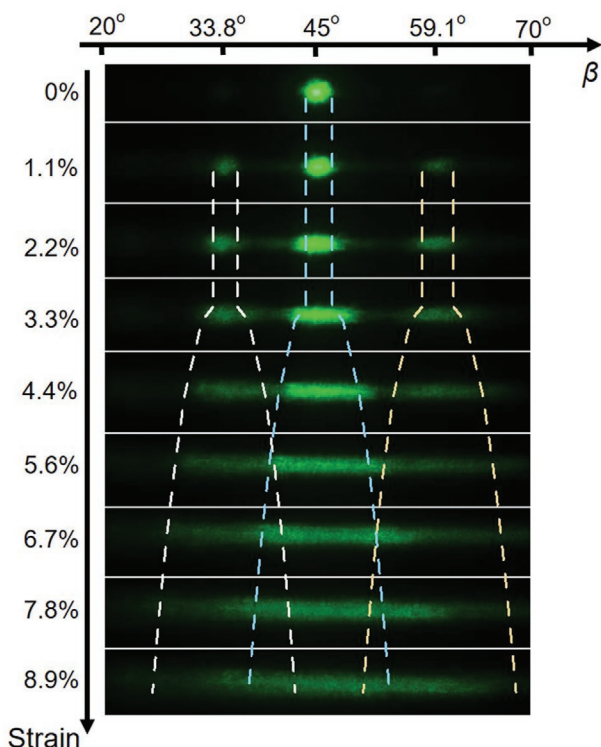


Figure 3. Laser reflective patterns from the thin film multilayer subject to successively increased compressive strain, ϵ . The wavelength of the incident laser λ_{laser} is 543 nm. The incident angle α is 45° . The angle to receive reflection is β . A screen with a normal direction β as 45° receives the reflective signals. The dashed lines indicate the plots of broadened angle $\Delta\beta \approx \sqrt{\epsilon - \epsilon_{\text{II}}}$, where ϵ_{II} is the critical strain of the broadening. The initial width of the diffraction pattern is included.

describe the details in Section 5. We relate diffraction broadening to the development of the hierarchical structures under a sequentially increased compressive strain (Figure 4).

Furthermore, we discover experimentally and model quantitatively that the morphology changes from hierarchical wrinkles with two periodicities (Figure 5a) to wrinkles with one large wavelength (Figure 5b). This change depends upon the multilayer properties and applied compression level. Our findings guide the rational design of wrinkling photonics with broad-angle iridescence and provide quantitative insight into how natural systems are specified to provide this attractive attribute.

3.1. Compression Induced Diffraction and Broadening

Compression of the thin film multilayer produces a reflection as shown in Figure 3. We summarize the material properties and the geometry of the multilayer in Table 1. Before compression, the reflection at $\beta = \alpha = 45^\circ$ is specular—no diffraction. With a compressive strain $\epsilon = 1.1\%$, two primary diffraction signals appear at the receiving angles $\beta = 33.8^\circ$ and 59.1° . When ϵ increases to 2.2%, the reflection only slightly broadens. At this stage, we infer a periodic grating structure has formed by the compression of the multilayer.

The reflectance broadens significantly when the compressive strain reaches 3.3%. When strain reaches 5.6%, the specular reflection signal and the diffraction signals interpenetrate. The intensity starts to decrease with further compression. At $\epsilon = 7.8\%$, the signals are homogenized, highly similar to the reflection of the iridescent part of *H. trionum* petals (Figure S1, Supporting Information). The tuning range of the observable angle reaches 20° by adjusting the applied compressive strain over a range of $\approx 9\%$ (Figure 3).

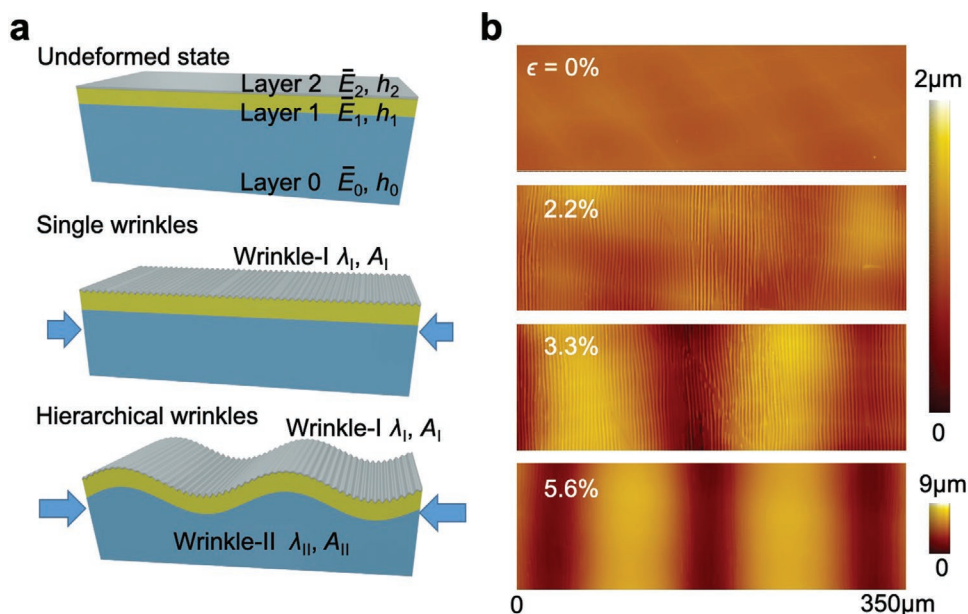


Figure 4. The development of surface morphologies of the thin film multilayer subject to compression. a) Schematics. The multilayer contains three layers of thin films. The plane-strain moduli are \bar{E}_0 , \bar{E}_1 , and \bar{E}_2 for the substrate layer, the middle layer, and the top layer, respectively. The thickness of each layer is h_0 , h_1 , and h_2 , respectively. The wavelength and amplitude of the small wrinkles are λ_I and A_I and that of the large wrinkles are λ_{II} and A_{II} . b) The surface morphologies observed through optical profilometry with successively increased compressive strain ϵ .

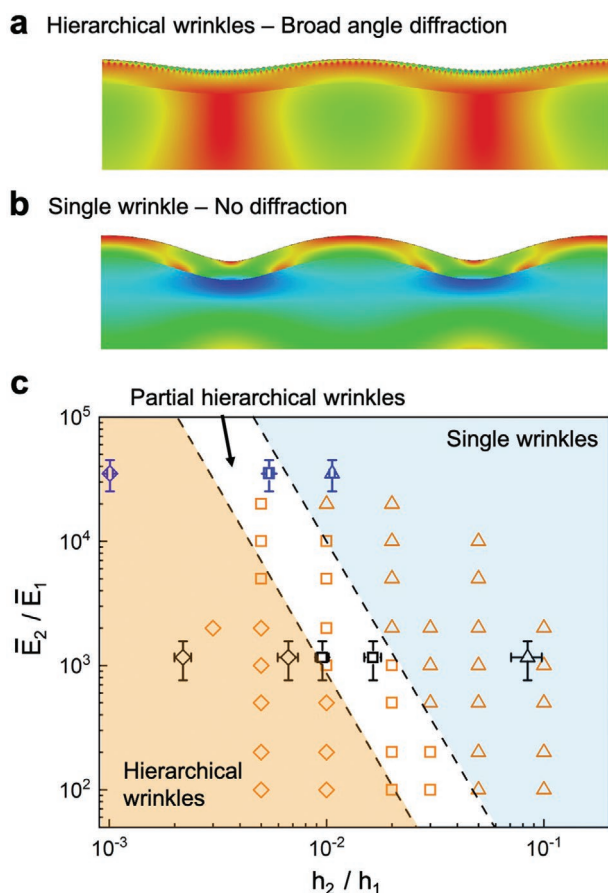


Figure 5. Collapse of hierarchical wrinkles to single wrinkles. A finite element calculation on a thin film multilayer with a) a hierarchical wrinkling mode and b) a single wrinkling mode. c) A diagram of hierarchical wrinkling mode and single wrinkling mode, as well as the transitional mode when the small wrinkles occur after the emergence of large wrinkles. The orange dots represent the calculated results through the finite element analysis. The black dots indicate the experimental results with polystyrene as the top layer material. The blue dots indicate the experimental results with gold as the top layer material. The diamonds represent the hierarchical wrinkles with broad-angle diffraction. The triangles represent the non-diffractive single wrinkles. The squares represent the intermediate mode of partial hierarchical wrinkles. The boundary line between the hierarchical wrinkling mode and the intermediate mode is $(\bar{E}_2/\bar{E}_1)(h_2/h_1)^3 = 4(\bar{E}_0/\bar{E}_1)^2$. The empirical boundary line between the single wrinkling mode and the transition mode follows $(\bar{E}_2/\bar{E}_1) \approx (h_2/h_1)^{-3}$. The plane-strain moduli mismatch between Layer-1 and Layer-0, \bar{E}_1/\bar{E}_0 , is 68.

The diffraction signal is largely reversible during unloading, but a weak residual narrow-band diffraction remains when the compression is completely released. This effect is likely due to the onset of plastic deformation in materials, as they are compressed beyond a critical strain.

3.2. Relating Optical Response to Wrinkling Mechanics

The broadening effect of diffraction can be directly related to the development of surface morphologies of the multilayer under compression as shown in Figure 4. Before compression, the surface is nearly flat to enable specular reflection. When a compressive strain ϵ reaches 1.1%, small wrinkles form. We label these small wrinkles that emerge first as wrinkle-I. The wavelength of the small wrinkles, denoted as λ_{I} , is $3.4 \pm 0.2 \mu\text{m}$. As ϵ increases to 2.2%, the amplitude of the small wrinkles increases. This morphology of small wrinkles is consistent with a periodic grating that gives rise to separated and narrow-angle diffraction signals, as shown in Figure 3.

When the multilayer is further compressed to $\epsilon = 3.3\%$, large wrinkles form in addition to the small wrinkles. We label these large wrinkles that emerge at larger strains as wrinkle-II. Their wavelength, denoted as λ_{II} , is $167 \pm 26 \mu\text{m}$, which is much larger than λ_{laser} and λ_{I} . Therefore, the large wrinkles do not interfere with the optical signal but tilt the normal direction of the grating surface. Hence, over a large area of reflection, the diffraction angle is broadened.

As compressive strain increases to 5.6%, we observe that the amplitude of the smaller wrinkles changes with respect to position along the larger wrinkles. Their amplitude decreases on the peaks and increases in the valleys of the larger wrinkles. This systematic distribution of the amplitude of small wrinkles reflects the stress distribution on the surface of the large wrinkles. As the large wrinkles amplify, the magnitude of compressive strain on the surface decreases near the peaks and increases in the valleys for wrinkle-II. This change in local compressive strain causes the wrinkle-I features to change in amplitude locally. Thus, these wrinkle-I changes decrease the diffraction intensity.

The onset compressive strain and wavelength for each level of wrinkles can be quantitatively predicted by applying a bilayer wrinkling theory^[39–42] to each set of bilayers within the multilayer composite. A comparison of experimental and theoretical values is provided in Table 1, along with the layers

Table 1. Hierarchical wrinkling properties of a synthetic multilayer as well as the properties of layers.

		Experiment	Bilayer wrinkling theory	Finite element analysis
Wrinkle-I	Critical strain, ϵ_1 [%]	<1.1	0.46 ± 0.11	0.55 ± 0.14
	Wavelength, λ_I [μm]	3.4 ± 0.2	2.83 ± 0.55	2.59 ± 0.52
Wrinkle-II	Critical strain, red ϵ_{II} [%]	$2.2 \approx 3.3$	3.12 ± 0.66	2.1 ± 0.2
	Wavelength, λ_{II} [μm]	167 ± 26	163.5 ± 22	188.5 ± 25
	Thickness		Young's modulus	Poisson's ratio
Layer-0 (PDMS(40:1))	186 ± 26 [μm]		33.0 ± 1.3 [kPa]	0.5
Layer-1 (PDMS(5:1))	9.19 ± 0.26 [μm]		2.25 ± 0.63 [MPa]	0.5
Layer-2 (Polystyrene)	61.3 ± 4.8 [nm]		3.17 ± 0.21 [GPa]	0.34

used in the bilayer theory to determine the theoretical values. Our precise control of individual layer properties and thicknesses (Table S1, Supporting Information) allows for this quantitative comparison.

The quantitative description of the hierarchical surface morphology allows the diffraction and broadening properties to be quantitatively connected to the multilayer structure and properties. We identify two key properties: the primary angles of diffraction and the broadened angles of each diffraction signal. Considering a grating surface with a periodicity, λ_1 , (Figure 1a) the angle to detect reflective signal satisfies the grating condition of diffraction,

$$\lambda_1(\sin \alpha - \sin \beta) = k\lambda_{\text{laser}} \quad (1)$$

where the integer k is a multiplier of the light wavelength.^[43] The terms on the left-hand side of Equation (1) determines the optical path difference reflected from the neighboring gratings. When the path difference matches an integer multiple of the optical wavelength, on the right-hand side of Equation (1), the interference becomes constructive. When $k = 0$, $\beta = \alpha = 45^\circ$, the reflection located in the center in Figure 3 is specular like a mirror. Note the specular reflection angle is independent of the optical wavelength and therefore non-selective to colors. $k = \pm 1$ indicates the primary diffraction detected in Figure 3. The experimental diffraction angles are $\beta = 33.8^\circ$ and 59.1° . With the measured grating periodicity, $\lambda_1 = 3.4 \pm 0.2 \mu\text{m}$ on this sample, the theoretical diffraction angles according to Equation (1) are $33.2^\circ \pm 0.6^\circ$ and $60.1^\circ \pm 1.1^\circ$, which agree well with the experimental measurement.

We analyze the broadening effect of diffraction related to the large wrinkles that tilt the grating surface. Consider a light incident to a tilted grating plane with a tilt angle θ (Figure S3, Supporting Information). With respect to the horizontal line, α and β become the nominal incident and receiving angles. The actual incident angle α' and receiving angle β' with respect to the tilted grating plane are adjusted such that $\alpha = \alpha' + \theta$ and $\beta = \beta' - \theta$. As the actual incident angle α' and receiving angle β' follow the grating equation (Equation (1)) to form diffraction, we can determine the nominal receiving angle β accordingly.

The tilt angle of the grating surface varies over a wavelength of the large wrinkles. The maximal tilt angle $|\theta_m|$ is governed by the aspect ratio of large wrinkles. The shape of the large wrinkles obeys a sinusoidal form, such that $\tan|\theta_m| = \pi A_{\text{II}}/\lambda_{\text{II}}$, where A_{II} is the amplitude and of the large wrinkle-II (Figure 4a). According to the bilayer wrinkling theory, the aspect ratio of the large wrinkles is $A_{\text{II}}/\lambda_{\text{II}} = (2/\pi)\sqrt{\varepsilon - \varepsilon_{\text{II}}}$. Therefore, taking the tilt angle θ between $-\theta_m$ and θ_m , we readily calculate the broadened receiving angle of $\Delta\beta$. To simplify the analysis, we take the aspect ratio of the large wrinkles to be small and approximate an explicit form of the broadened angle of diffraction:

$$\Delta\beta = 4 \left(1 + \frac{\cos \alpha}{\sqrt{1 - (k\lambda_{\text{laser}}/\lambda_{\text{II}} - \sin \alpha)^2}} \right) \sqrt{\varepsilon - \varepsilon_{\text{II}}} \quad (2)$$

Equation (2) characterizes the limits of the broadened angles as the tilt angle reaches its maximum. Essentially, $\Delta\beta \approx \sqrt{\varepsilon - \varepsilon_{\text{II}}}$,

which is plotted as dashed lines in Figure 3. This scaling describes the broadening effect well. Accordingly, the tuning accuracy of the observable angles is set by the accuracy of the applied compressive strain. In our system, the strain accuracy is $\approx 0.1\%$, which corresponds to an observable angle range accuracy of 0.2° .

Based on the specific history of applied compressive strain used in our approach, the hierarchical structure and the associated optical effect remain stable when the system is released from the mechanical apparatus. Even though we use elastic materials, the thin film multilayer is naturally compressed by the prestrained mounting layer substrate. Alternatively, different materials could be selected to permanently fix the hierarchical structure if different strain histories are preferred. For example, the multilayer could be an elastomer that can be crosslinked after wrinkle formation, as demonstrated previously for single wavelength surface wrinkles.^[44,45]

3.3. Structure and Process Controlled Limits

The development of reflective diffraction across an enhanced angular range only exists for a finite range of structures and processing conditions. In other words, for multilayers with individual constituents that do not have appropriately tuned mechanical responses, a single wrinkle with one wavelength will develop upon compression. We observed evidence of this limited range experimentally. For example, when we reduce the thickness of Layer 1 from $9.19 \mu\text{m}$ to $0.732 \mu\text{m}$ and keep all other layers the same as in Table 1, the small wrinkles disappear (Figure S4a, Supporting Information). The same single wrinkling mode also occurs when we change Layer 2 from a polystyrene film to a 50 nm-thick gold film and keep other layers the same as in Table 1 (Figure S4b, Supporting Information). A laser reflection experiment on a single wrinkling surface with a large wavelength does not show a diffraction signal (Figure S4c, Supporting Information). Also, similar limitations are observed in natural systems. For example, the iridescent part of *H. trionum* petals is limited to the proximal region where the cuticle forms nano-ridges (Figure 2b–d, Region 1 in Figure S1, Supporting Information). Meanwhile, the distal part of the petal is not iridescent and the cuticle on the epidermal cells is smooth without striations (Region 3 in Figure S1, Supporting Information).

We used a numerical model to understand these boundaries for defining multilayer composites that will develop hierarchical wrinkles. We describe the details in Section 5. We considered the variance of three dimensionless parameters that represent the thicknesses and moduli mismatch between layers as governing parameters: h_2/h_1 , \bar{E}_2/\bar{E}_1 , and \bar{E}_1/\bar{E}_0 , where h_i denotes the layer thickness, \bar{E}_i denotes the plane-strain modulus, and the subscript i represents the layer index marked as in Figure 4a. We neglect the finite thickness effect of Layer 0, h_0 . Therefore, in this limit, hierarchical wrinkles (Figure 5a) with enhanced reflection diffraction angles develop primarily when h_2 is less than h_1 by a critical ratio related to the elastic moduli mismatch \bar{E}_1/\bar{E}_0 (Figure 5c).

We developed an analytical relationship for this boundary by setting the critical strain for bilayer wrinkling for Layer 1

and Layer 2 equal to the critical strain for wrinkling a bilayer comprised of a composite layer and Layer 0. In the regime of single wrinkling, a bilayer composite comprises Layers 1 and 2 to wrinkle on the substrate Layer 0 (Figure 5b).^[46,47] The elastic properties of the composite are characterized by its stretching modulus \bar{E}_S and bending modulus \bar{E}_B , both associated with the modulus and thickness of each layer.^[48] The critical strain of the single wrinkling of the composite layer is $(3\bar{E}_0/\bar{E}_B)^{2/3}(\bar{E}_B/4\bar{E}_S)$. In the regime of hierarchical wrinkling, the small wrinkles trigger first and lead to the hierarchical wrinkling. As the full analysis of the small wrinkling of Layer 2 on the composite substrate with Layers 1 and 0 was carried out by Jia et al.,^[48] we simplify the onset dictated by the bilayer wrinkling of Layer 2 on Layer 1, which gives the critical strain of the small wrinkling $(3\bar{E}_1/\bar{E}_2)^{2/3}/4$. By comparing the critical strains for these two wrinkling modes, we readily obtain the line of equivalence for the critical strains. In the limit of $\bar{E}_2 \gg \bar{E}_1$, $h_2 \ll h_1$, and $\bar{E}_2 h_2 > \bar{E}_1 h_1$, this critical strain equivalence condition simplifies to be: $(\bar{E}_2/\bar{E}_1)(h_2/h_1)^3 = 4(\bar{E}_0/\bar{E}_1)^2$. This line is plotted as the boundary line in Figure 5c, which shows excellent agreement with the numerical and experimental data that define the wrinkling morphologies. This line also precisely captures the mode transition demonstrated in Jia et al.^[48]

Beyond this boundary, the large wrinkles form before the surface shows any diffractive small wrinkles. Within a certain limit, the small wrinkles show partially in the valleys of large wrinkles where there is a concentration of compressive strain. The boundary between the transitional partial hierarchical wrinkling and single wrinkling is beyond the analytical model. Empirically, we find the scaling of this boundary line defined by the experiments and simulations follows $\bar{E}_2/\bar{E}_1 \approx (h_2/h_1)^{-3}$.

Interestingly, for systems where hierarchical wrinkling is favored at low strains, a limit of partial hierarchical wrinkling is also found for high strains. In these systems, the strain distribution is set by the larger wrinkle waveform and disrupts the uniformity of small wrinkle amplitudes. This disruption causes the reflection diffraction pattern to also decrease in intensity. These transitions are beyond the capabilities of analytical modeling, but our experiment and numerical model provide insight into how this disruption develops at large strains. As the large wrinkles amplify with the increased compression, the magnitude of compressive strain on the surface decreases around the peaks and increases in the valleys of large wrinkles. The amplitude of the small wavelength decreases and even disappears due to the loss of compressive strain near the peaks. Similar surface morphologies were investigated on a buckled free-standing thin film bilayer.^[39,49] Therefore, under very high strains, the loss of the majority of small wrinkles (except the very limited amount in the valleys) effectively reduces the intensity of the optical diffraction.

Importantly, this new knowledge not only provides technological advances for materials design but also helps to identify the limits for natural systems. For example, the material properties of the cuticle layer relative to the plant cell wall must fall within a specified range to allow for hierarchical wrinkling in the proximal parts. Additionally, the compressive strains induced during cuticle production must not exceed a critical value that would lead to non-uniform amplitudes in the small scale wrinkles. These predictions help to frame new

measurements in plant science and provide guidelines in developing new experiments to identify factors that may disrupt natural wrinkling in plants.

4. Conclusion

We have presented a tunable design of hierarchical wrinkles on thin film multilayers to harness the broadening mechanism of structural color. We utilized mechanical hierarchical wrinkling as the fabrication method to achieve complex, controlled hierarchical structures over a large area and with efficiency. We related the diffraction features to the development of the hierarchical structures under a sequentially increased compressive strain. We found that the small wrinkles govern the primary diffraction angle following the grating interference theory, and the large wrinkles broaden the diffraction signals.

A primary advantage of this system, as supported by our theoretical model, is that the broadening of the diffraction signal can be systematically tuned by the applied compressive strain. Our experiments and models also demonstrate that this enhanced control is only available for a limited range of elastic moduli, layer thicknesses, and compressive strains. Taken together, this new quantitative understanding is anticipated to guide the selection of materials and conditions for photonic devices with real-time tuning capabilities.

5. Experimental Section

Experimental Section is included in the Supporting Information.

Supporting Information

Supporting Information is available from the Wiley Online Library or from the author.

Acknowledgements

The authors thank Prof. James Watkins for the use of the Zygo profilometer and Prof. Thomas McCarthy for the use of the ellipsometer. The authors thank Dr. Yongjin Kim for help with wrinkling experiments, Matthew Dorling for excellent plant care, and Jordan Ferria for useful discussions. The work is supported by the Human Frontier Science Program (HFSP, No. RGP0019/2017).

Conflict of Interest

The authors declare no conflict of interest.

Keywords

broad-angle diffraction, hierarchical wrinkling, multilayer wrinkling

Received: July 24, 2020
Revised: October 8, 2020
Published online:

- [1] K. Nassau, *The Physics and Chemistry of Color: The Fifteen Causes of Color*, Wiley Series in Pure and Applied Optics, Wiley, New York **2001**.
- [2] D.-P. Song, T. H. Zhao, G. Guidetti, S. Vignolini, R. M. Parker, *ACS Nano* **2019**, *13*, 1764.
- [3] S. Kinoshita, S. Yoshioka, *ChemPhysChem* **2005**, *6*, 1442.
- [4] S. Kinoshita, S. Yoshioka, J. Miyazaki, *Rep. Prog. Phys.* **2008**, *71*, 076401.
- [5] Y. D. Afanasyev, G. T. Andrews, C. G. Deacon, *Am. J. Phys.* **2011**, *79*, 1079.
- [6] H. M. Whitney, M. Kolle, P. Andrew, L. Chittka, U. Steiner, B. J. Glover, *Science* **2009**, *323*, 130.
- [7] P. Vukusic, J. Sambles, C. Lawrence, R. Wootton, *Proc. R. Soc. London, Ser. B* **1999**, *266*, 1403.
- [8] B.-K. Hsiung, R. H. Siddiqui, D. G. Stavenga, J. C. Otto, M. C. Allen, Y. Liu, Y.-F. Lu, D. D. Deheyne, M. D. Shawkey, T. A. Blackledge, *Nat. Commun.* **2017**, *8*, 2278.
- [9] A. E. Seago, P. Brady, J.-P. Vigneron, T. D. Schultz, *J. R. Soc., Interface* **2009**, *6*, S165.
- [10] H. Yin, L. Shi, J. Sha, Y. Li, Y. Qin, B. Dong, S. Meyer, X. Liu, L. Zhao, J. Zi, *Phys. Rev. E* **2006**, *74*, 051916.
- [11] D. G. Stavenga, H. L. Leertouwer, N. J. Marshall, D. Osorio, *Proc. R. Soc. B* **2011**, *278*, 2098.
- [12] J. Teyssier, S. V. Saenko, D. v. d. Marel, M. C. Milinkovitch, *Nat. Commun.* **2015**, *6*, 6368.
- [13] S. Fitzpatrick, *JSTOR* **1998**, *35*, 67.
- [14] D. Stuart-Fox, M. J. Whitting, A. Moussalli, *Biol. J. Linn. Soc.* **2006**, *88*, 437.
- [15] C. Héban, D. W. Lee, *Am. J. Bot.* **1984**, *71*, 216.
- [16] S. Vignolini, P. J. Rudall, A. V. Rowland, A. Reed, E. Moyroud, R. B. Faden, J. J. Baumberg, B. J. Glover, U. Steiner, *Proc. Natl. Acad. Sci.* **2012**, *109*, 15712.
- [17] E. Moyroud, T. Wenzel, R. Middleton, P. J. Rudall, H. Banks, A. Reed, G. Mellers, P. Killoran, M. M. Westwood, U. Steiner, S. Vignolini, B. J. Glover, *Nature* **2017**, *550*, 469.
- [18] M. Vatankhah-Varnosfaderani, A. N. Keith, Y. Cong, H. Liang, M. Rosenthal, M. Sztucki, C. Clair, S. Magonov, D. A. Ivanov, A. V. Dobrynin, S. S. Sheiko, *Science* **2018**, *359*, 1509.
- [19] K. Katagiri, Y. Tanaka, K. Uemura, K. Inumaru, T. Seki, Y. Takeoka, *NPG Asia Mater.* **2017**, *9*, e355.
- [20] W. Fan, J. Zeng, Q. Gan, D. Ji, H. Song, W. Liu, L. Shi, L. Wu, *Sci. Adv.* **2019**, *5*, eaaw8755.
- [21] T. Park, S. Yu, S. Cho, H. Kang, Y. Kim, M. Kim, H. Eoh, C. Park, B. Jeong, S. Lee, D. Ryu, J. Huh, C. Park, *NPG Asia Mater.* **2018**, *10*, 328.
- [22] H. J. Park, T. Xu, J. Y. Lee, A. Ledbetter, L. J. Guo, *ACS Nano* **2011**, *5*, 7055.
- [23] K. Chung, S. Yu, C.-J. Heo, J. W. Shim, S.-M. Yang, M. G. Han, H.-S. Lee, Y. Jin, S. Y. Lee, N. Park, J. H. Shin, *Adv. Mater.* **2012**, *24*, 2375.
- [24] S. Vignolini, E. Moyroud, T. Hingant, H. Banks, P. J. Rudall, U. Steiner, B. J. Glover, *New Phytol.* **2015**, *205*, 97.
- [25] R. L. Antoniou Kourounioti, L. R. Band, J. A. Fozard, A. Hampstead, A. Lovrics, E. Moyroud, S. Vignolini, J. R. King, O. E. Jensen, B. J. Glover, *J. R. Soc., Interface* **2013**, *10*, 20120847.
- [26] Z.-C. Shao, Y. Zhao, W. Zhang, Y. Cao, X.-Q. Feng, *Soft Matter* **2016**, *12*, 7977.
- [27] M. I. Abid, L. Wang, Q.-D. Chen, X.-W. Wang, S. Juodkakis, H.-B. Sun, *Laser Photonics Rev.* **2017**, *11*, 1600187.
- [28] G. Lin, P. Chandrasekaran, C. Lv, Q. Zhang, Y. Tang, L. Han, J. Yin, *ACS Appl. Mater. Interfaces* **2017**, *9*, 26510.
- [29] S. Schauer, M. Worgull, H. Hölscher, *Soft Matter* **2017**, *13*, 4328.
- [30] G. Chu, A. Camposeo, R. Vilensky, G. Vasilyev, P. Martin, D. Pisignano, E. Zussman, *Matter* **2019**, *1*, 988.
- [31] J. H. Oh, J. Y. Woo, S. Jo, C.-S. Han, *ACS Appl. Mater. Interfaces* **2019**, *11*, 26442, pMID: 31145579.
- [32] K. Efimenko, M. Rackaitis, E. Manias, A. Vaziri, L. Mahadevan, J. Genzer, *Nat. Mater.* **2005**, *4*, 293.
- [33] J.-Y. Sun, S. Xia, M.-W. Moon, K. H. Oh, K.-S. Kim, *Proc. R. Soc. A* **2012**, *468*, 932.
- [34] Y. Liu, M. Li, J. Liu, X. Chen, *J. Appl. Mech.* **2017**, *84*, 051011.
- [35] Z. Chen, X. Zhang, J. Song, *Soft Matter* **2018**, *14*, 8717.
- [36] L. Pellegrino, S. Khodaparast, J. T. Cabral, *Soft Matter* **2020**, *16*, 595.
- [37] J.-H. Lee, H. Ro, R. Huang, P. Lemaillet, T. A. Germer, C. L. Soles, C. M. Stafford, *Nano Lett.* **2012**, *12*, 5995.
- [38] J. J. Richardson, M. Bjornmalm, F. Caruso, *Science* **2015**, *348*, aaa2491.
- [39] H. G. Allen, *Analysis and Design of Structural Sandwich Panels*, Pergamon Press, Oxford, UK **1969**.
- [40] N. Bowden, S. Brittain, A. G. Evans, J. W. Hutchinson, G. M. Whitesides, *Nature* **1998**, *393*, 146.
- [41] X. Chen, J. W. Hutchinson, *J. Appl. Mech.* **2004**, *71*, 597.
- [42] Z. Huang, W. Hong, Z. Suo, *J. Mech. Phys. Solids* **2005**, *53*, 2101.
- [43] E. G. Loewen, E. Popov, *Diffraction Gratings and Applications*, CRC Press, New York **1997**.
- [44] E. Chan, E. Smith, R. Hayward, A. Crosby, *Adv. Mater.* **2008**, *20*, 711.
- [45] Y.-C. Chen, Y. Wang, T. J. McCarthy, A. J. Crosby, *Soft Matter* **2017**, *13*, 4142.
- [46] A. J. Nolte, R. E. Cohen, M. F. Rubner, *Macromolecules* **2006**, *39*, 4841.
- [47] R. Huang, C. M. Stafford, B. D. Vogt, *J. Aerospace Eng.* **2007**, *20*, 38.
- [48] F. Jia, Y.-P. Cao, T.-S. Liu, Y. Jiang, X.-Q. Feng, S.-W. Yu, *Philos. Mag.* **2012**, *92*, 1554.
- [49] S. Nikravesh, D. Ryu, Y.-L. Shen, *Sci. Rep.* **2020**, *10*, 5728.